Microscopic contact line dynamics dictate the emergent behaviors of particle rafts

Ranit Mukherjee and Zih-Yin Chen*
Department of Mechanical Engineering, University of Minnesota, Minneapolis 55455, Minnesota, USA

Xiang Cheng
Department of Chemical Engineering and Materials Science, University of Minnesota, Minneapolis 55455, Minnesota, USA
and St. Anthony Falls Laboratory, University of Minnesota, Minneapolis 55414, Minnesota, USA

Sungyon Lee†
Department of Mechanical Engineering, University of Minnesota, Minneapolis 55455, Minnesota, USA
and St. Anthony Falls Laboratory, University of Minnesota, Minneapolis 55414, Minnesota, USA

(Received 3 December 2024; accepted 18 July 2025; published 20 August 2025)

Fluid-fluid interfaces laden with discrete particles behave curiously like continuous elastic sheets, leading to their applications in emulsion and foam stabilization. Although existing continuum models can qualitatively capture the elastic buckling of these particle-laden interfaces, often referred to as particle rafts, under compression, they fail to link their macroscopic collective properties to the microscopic behaviors of individual particles. Thus, phenomena such as particle expulsion from the compressed rafts remain unexplained. Here, by combining systematic experiments with first-principle modeling, we reveal how the macroscopic mechanical properties of particle rafts emerge from particle-scale interactions. We construct a phase diagram that delineates the conditions under which a particle raft collapses via collective folding versus single-particle expulsion. Guided by this theoretical framework, we demonstrate control over the raft's failure mode by tuning the physicochemical properties of individual particles. Our study highlights the dual nature of particle rafts and exemplifies how collective dynamics can arise from discrete components with simple interactions.

DOI: 10.1103/ld9n-ctdh

I. INTRODUCTION

If we keep on adding millimeter-sized dense particles to a fluid-fluid interface to cover the entire interface eventually, two things happen: first, the monodisperse particles stabilize at the interface to form a neat hexagonal lattice structure, and second, perhaps more surprisingly, the interface achieves a remarkable elasticity [1–7], behaving similarly to a floating elastic sheet at a fluid surface [8,9] (see Supplemental Material [10], movies S1 and S3). The ability of a particle-laden interface to resist a compressive stress via out-of-plane wrinkles and folds underpins their numerous technological applications, ranging from the stabilization of fluid-fluid interfaces [11–14] to the formation of bijels [15–17]. In contrast, a jammed particle-laden interface can also "relieve" stress by ejecting

*Present address: Department of Mechanical Engineering, National Taiwan University, Taipei City, Taiwan 10617.
†Contact author: sungyon@umn.edu

individual particles from the interface instead of a collective out-of-plane deformation [18,19] (Supplemental Material, movie S1). While this behavior can be utilized in applications involving the controlled release of particles in biomass conversion and gas storage [20,21], it fundamentally points to the inherent granular characteristics of particle-laden interfaces. This, perhaps, makes particle-laden interfaces the simplest composite material. A deeper understanding of the transition between these mutually exclusive behaviors of particle rafts could enable more precise design and control of their dynamics, tailored to specific applications.

Despite early reports of buckling-to-particle expulsion transition in particle-laden interfaces [22,23], existing continuum models [24] focused mainly on explaining the interface buckling behavior [25]. More recent simulations and analytical studies have attempted to understand the transition through individual particle interactions at the interface [26–28]. However, these analyses ignore the crucial effects of surface hysteresis [29] or particle size [26] in particle-fluid interactions at the interface, despite evidence to the contrary [30]. Other variations of the slender elastic beam model, initially developed by Vella and Mahadevan for planar particle rafts [24], have also failed to account for their granular characteristics [6,7,31–33], including particle expulsion observed during uniaxial compression in a Langmuir troughlike setup [34]. Interestingly, Ref. [34] mentions particle expulsion only as a limitation of their continuum model that assumes the raft remains jammed with a fixed number of particles.

A recent study from our group attempted to circumvent the inherent limitations of a continuum model by allowing the particle concentration along the interface to vary and using the resultant shape of the one-dimensional (1D) raft as a proxy for different failure modes [19]. While this could qualitatively capture the buckling and expulsion events in our experiments, it failed to incorporate the physicochemical properties of individual particles, ultimately joining the long list of continuum models that cannot make sense of raft granularity.

Recognizing the fundamental limitation of a continuum model to describe the granular characteristics of rafts, we aim to develop a unifying model that provides a physical explanation for their dual nature. Building upon the existing continuum analysis [34], we explain raft behaviors as the competition between the energy required to detach a single particle and the energy needed to buckle the entire interface. By minimizing the energy of the particle-fluid system, the continuum model produces a term analogous to the *ad hoc* bending modulus proposed in previous studies. We also establish a physical picture of collective raft behaviors by incorporating the evolving shape of the meniscus around the individual particles. Finally, guided by the model prediction on the microscale-macroscale relationship, we demonstrate the capability of engineering raft behaviors by altering the contact line dynamics of individual particles at the fluid interface.

The paper is organized as follows: We introduce the experimental setups for the raft compression experiments and particle-scale measurements, and summarize the experimental observations in Sec. II. We develop the model and make the quantitative comparison with the experiments in Sec. III, in addition to altering the raft's failure mode via surface roughness in Sec. IV. Finally, we conclude the paper with a summary and an outline of future work in Sec. V.

II. EXPERIMENTS

A. Compression experiments

We quasistatically compress a particle raft formed between two fluids (a lower fluid with density ρ_1 and an upper fluid with density ρ_2) to the point of failure. The particles used in this study are made of soda-lime glass (Ceroglass, density $\rho_p \approx 2500\,\mathrm{kg/m^3}$). They come in different ranges of diameters d: the minimum diameter range is 80–100 μm and the maximum is $d = 1250$–1650 μm. We include the details of particles and fluids used in our experiments in Appendix A. To form a particle raft, we gently sprinkle particles onto a surface of fluid 1 (water or brine) from a height of ∼2–5 cm from the interface. We ensure that the height from which the particles are released remains consistent, as the release height is shown to affect the final equilibrium position of the particles. We

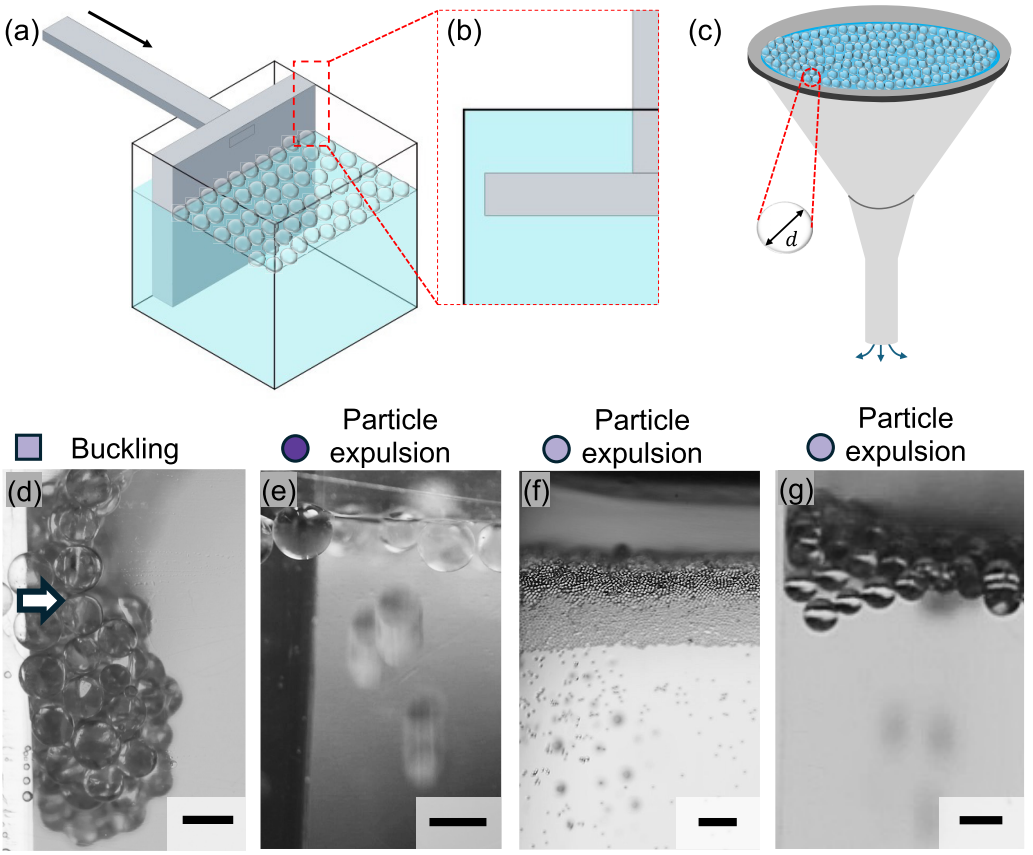

FIG. 1. Compression experiment setups. (a) A square acrylic chamber and plunger were used as a trough for compression experiments. The end of the plunger shaft away from the chamber is attached to a syringe pump pusher block. (b) Inset shows the ∼1-mm gap between the chamber and the plunger to allow for liquids to escape from the front. (c) Biaxial compression of rafts is achieved in a funnel by draining the liquid. Failure of particle rafts under compression. (d) Side view of a granular raft that fails through buckling (denoted by a square at the top) at a hexane-water interface ($\Delta\rho = 345\,\mathrm{kg/m^3}$) during compression in a trough. The white arrow indicates the direction of compression. (e) A raft made of similarly sized particles fails via single-particle expulsion (denoted by a circle) at an air-water interface ($\Delta\rho = 999\,\mathrm{kg/m^3}$). While keeping the interfacial fluid combination the same as the hexane-water interface, buckling to particle-expulsion transition can also be obtained (f) by reducing the particle diameter from $d \approx 900$ to 90 μm or (g) by making the particle surface more hydrophilic.

also take care not to add all the particles at once so that only a monolayer of particles is formed at the interface. As the individual particles are heavier than the fluid, they quickly settle onto the interface, finding their equilibrium positions. In the experiments where fluid 2 is also liquid (i.e., hexane), we gently add fluid 2 on top of the raft, ensuring that we do not disturb the particle raft that has been formed. For particles smaller than $d < 500$ μm, fluid 2 is added prior to the addition of particles, which helps minimize particle clumping.

Two different experimental setups are used for observing raft dynamics in compression: a square trough and a funnel. The square trough is an open-top acrylic chamber (Amazon) that compresses a raft uniaxially in the direction shown with an arrow [see Fig. 1(a)]. The transparent and flat walls of the chamber allow for a detailed view of rafts and individual particles. Compression is achieved with

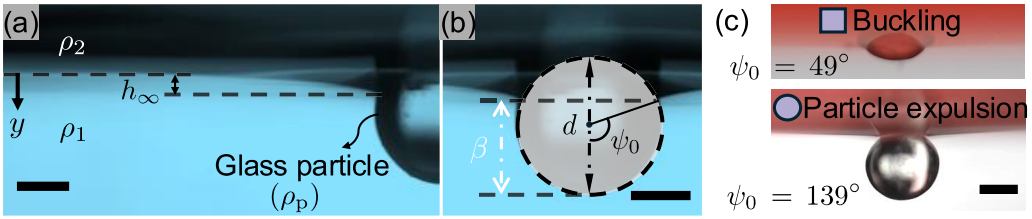

FIG. 2. (a) Particle with density ρ_p floating at a fluid-fluid interface with densities ρ_1 and ρ_2. All the distances are measured from the undisturbed horizontal interface far from the particle. The solid-fluid contact line is h_∞ distance away. (b) The particle equilibrium position at an interface is given by ψ_0, the angle between the center line of the particle and the contact line; β is the fraction of the particle below the contact line within the lower fluid. (c) When the particle position at a hexane-water interface changes from $\psi_0 = 49°$ to $139°$, the corresponding raft failure mode changes from buckling to single-particle expulsion. Scale bars in all the images denote 1 mm.

a moving plate attached to the pusher block of a syringe pump (KD Scientific, Model LEGATO110) using a shaft. For all compression experiments in the trough, a flow rate of 3 mL/min is used, which translates to a linear speed of 55 μm/s. The width of the compressing plate is slightly smaller (≈0.5 mm on each side) than the internal width of the acrylic chamber, as shown in Fig. 1(b). This ensures that when the raft is compressed, the fluid level stabilizes on either side of the plunger. In the experiments with smaller particles (90–350 μm), few particles also escape from this gap but do not affect the overall compression of the system. The funnel setup is similar to the one used in [19] and illustrated in Fig. 1(c). The biaxial compression of rafts is achieved by draining the lower fluid at a specific rate ($\dot{Q} = 50$ mL/min) via a syringe pump.

Results from these methods are used interchangeably as they are quantitatively similar. Our experimental observations establish the essential roles of fluid densities ($\Delta\rho = \rho_1 - \rho_2$), particle diameter ($d$), and particle surface wettability in determining the raft failure modes during compression (see Supplemental Material, movie S2). Rafts predominantly fail via particle expulsion for higher $\Delta\rho$, as shown by the transition from buckling at a hexane-water interface [Fig. 1(d)] to particle expulsion at an air-water interface in Fig. 1(e). Moreover, at the same hexane-water interface, when the particle diameter is reduced [Fig. 1(f)] or the particle surface is made more hydrophilic [Fig. 1(g)], a similar transition from buckling to particle expulsion can be observed. Although the effects of fluid densities and particle diameter on raft properties and behaviors have been reported previously [6,19,24,33], the exact role of the surface wettability on raft dynamics remains an open question [6,7], which leads to an incomplete understanding of particle raft behaviors.

B. Extracting individual particle information to understand raft behavior

To understand the relationship between particle surface wettability and raft failure modes, we visualize the individual particles and extract their static equilibrium position on a given fluid surface as shown in Fig. 2(a). For these individual particle experiments, we directly measure the particle diameter for each experiment, instead of relying on the mean value. Hence, in some cases, the particle diameters in the individual particle experiments may deviate from the mean values included in Appendix A. For particles smaller than $d < 500$ μm, lighter fluids are added before the particles are placed at the interface inside a rectangular acrylic chamber with dimensions 6.5 cm × 3 cm × 2.5 cm. An in-house vacuum-controlled "tweezer" is used to handle a single particle carefully. The tweezer is a syringe barrel with a hollow needle at the end connected to the vacuum pump via a flexible tube. Once the pump is turned on, the tube, barrel, and hollow needle stay in suction mode. Using an appropriate needle gauge (15 or 21 GA) according to the particle size, we pick up one particle at a time with this mechanism and subsequently release it by turning off the pump and opening the pump valve. Using an adjustable steel platform on

which the chamber is placed, we keep the distance between the needle holding the particle and the experimental chamber consistent at $\lesssim$6 mm, so that the particle release height does not change between the experiments. Once the particle falls onto the interface, we allow approximately 1 min for the system to equilibrate before taking an image using a camera with a macro lens (Canon Mark IV, fitted with a 65 mm 1–5× zoom). Three different particles are used to extract a reliable mean for each fluid-fluid interface and particle size.

We define the static equilibrium position by the angle ψ_0 between the particle centerline and the three-phase contact line [Fig. 2(b)]. The fraction of the particle below the three-phase contact line is given by $\beta \equiv (1/2)(1 - \cos\psi_0)$, which can vary from $\beta = 1$ (full submersion into fluid 1) to $\beta = 0$ (zero submersion). The value of β depends on the particle weight (i.e., d, ρ_p), fluid densities, and surface tension, as well as the wettability of the particle surface, which will be detailed below. For instance, for the same particle and fluid properties, increasing the particle wettability to fluid 1 would cause the particle to be more submerged into the lower fluid, leading to an increase in β. The location of the contact line can also be denoted by the length h_∞ measured from the undisturbed fluid-fluid interface.

As expected, the surface wettability of the particles plays a vital role in determining their static equilibrium positions at a fluid-fluid interface. When a cleaned glass bead of diameter ≈900 μm is placed on a hexane-water interface, the majority of the particle stays within the hexane phase with $\psi_0 = 49^\circ$ [Fig. 2(c) top panel]. In contrast, when uncleaned particles of the same size are placed at the hexane-water interface, ψ_0 is increased to 139° [Fig. 2(c) bottom panel]. The hydrophilicity of the uncleaned particles is probably a result of soda-lime glass surfaces acquiring a micrometric thin layer of water film in a humid environment [35]. We observe that rafts of clean $d \approx 900\,\mu$m particles fail via buckling, while rafts of hydrophilic particles of the same size fail through single-particle expulsion.

To further test if the static equilibrium position of the particles at the interface effectively controls the raft dynamics, we also increase ψ_0 of a clean particle by adding surfactant in the water phase. As surface tension γ is lowered from 43 to 14 mN/m, ψ_0 increases to 137°. Again, the raft at this modified interface fails via particle expulsion, demonstrating the crucial role of individual particles' equilibrium position in determining the raft dynamics under compressive loading.

III. MODEL

A. Battle of two energies: A modified continuum model for interface buckling

Our experimental observations require a model that can simultaneously capture the granular and elastic nature of the raft and explain the effects of three key physical parameters (fluid densities, particle size, and equilibrium particle position) on the raft's failure. Rather than performing computationally expensive grain-scale simulations, we develop two distinct simplified models: one that treats the particle raft as an elastic sheet and another that isolates a single particle at the interface. Using the two models, we compare the energies required for each failure mode: system-wide buckling and particle expulsion as a function of the key physical parameters. We hypothesize that the competition between the two energies determines the failure mode of particle rafts.

For the collective buckling of the particle-laden interface, we model the raft as a 1D continuous sheet by considering an array of spherical particles in the intrinsic coordinates (s, α), where s is the arclength and α is the angle between the line tangent to the array and the horizontal axis x [Figs. 3(a) and 3(b)]. We will follow the floating elastic sheet model used previously by Jambon-Puillet [34] with a small but significant caveat: unlike the previous studies that used the beam equation to model the buckling of rafts [3,6,36,37], we will not rely on an *ad hoc* bending modulus. Instead, we derive the equation for the shape of the compressed particle raft via energy minimization at a given compression level Δ. We shall see that an effective bending modulus can be derived directly from this physical understanding.

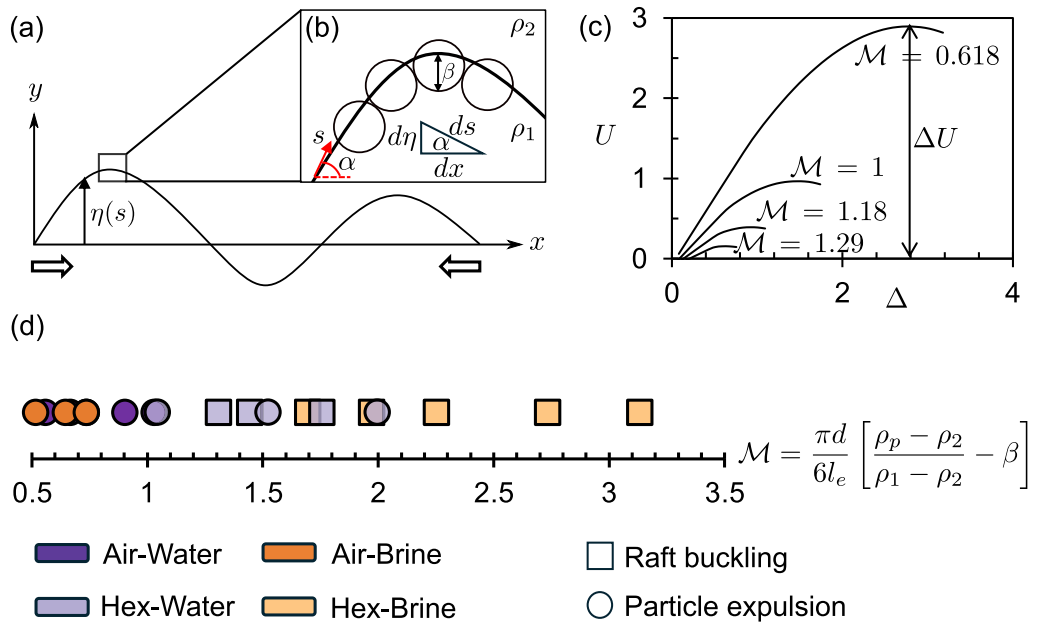

FIG. 3. A model for the particle raft failure. (a), (b) The continuum model of the raft is a one-dimensional array of spheres constrained in the (x, y) plane between two fluids with densities ρ_1 and ρ_2. The vertical distance denotes raft deformation, $\eta(s)$, where (s, α) are the intrinsic coordinates for energy calculations and the equilibrium equation. (c) Variation of the dimensionless total raft energy U with raft compression Δ, for given $\mathcal{M}$. ΔU denotes the energy barrier for buckling the particle raft. (d) The experimental results at four different fluid-fluid interfaces are plotted against a dimensionless mass parameter $\mathcal{M}$. Although increasing $\mathcal{M}$ may seem to indicate a transition from the particle expulsion to buckling mode of failure, both failure modes are observed between $1.5 < \mathcal{M} < 2$.

The total energy of the raft comprises contributions from the potential energy of the particles, U_p, the potential energy of the fluids, U_f, and the interfacial energy between the two fluids and the particles, U_i. In the above coordinate system, these energies will have the following forms:

$$U_p = (\rho_p - \rho_2)g(1-\beta)\forall_p\phi_s \int_0^L (\eta + CG_2)\, ds + (\rho_p - \rho_1)g\beta\forall_p\phi_s \int_0^L (\eta - CG_1)\, ds, \tag{1a}$$

$$U_f = \frac{(\rho_1 - \rho_2)gd}{2} \int_0^L \eta^2 \cos(\alpha)\, ds, \tag{1b}$$

$$U_i = \frac{\pi d^2 \gamma \phi_s}{2} \int_0^L \left[1 + \cos^2\theta_{\text{eq}} + \frac{3d^2(\partial_s \alpha)^2}{8} \sin^4\theta_{\text{eq}}\right] ds, \tag{1c}$$

where $\forall_p = \pi d^3/6$ is the volume of a spherical particle, $\phi_s = 1/d$ is the number of particles per unit length along s under a jammed condition, and CG_1 and CG_2 are the vertical distances of the particle centroid below and above the contact line, respectively. Notably, U_i corresponds to the change in the total interfacial energy of a curved particle-laden interface relative to the flat counterpart, while the particles are assumed to remain pinned on the interface [6,29,38,39].

We choose a characteristic length $\ell_e \equiv (K/\Delta\rho g)^{1/4}$ and an equivalent energy Kd/ℓ_e to nondimensionalize Eq. (1), where $K \equiv (3\pi/8)\gamma d^3 \phi_s \sin^4\theta_{\text{eq}}$. We set the value of the equilibrium contact angle θ_{eq} based on independent wettability measurements using a glass slide (experimental details are provided in Appendix B and Fig. 6). Next, we establish the physical meaning behind our choice of scaling length ℓ_e and energy K. By differentiating the interfacial energy U_i with the curvature

α, we obtain a bending modulus $B \equiv (3\pi/8)\gamma d^3\phi_s \sin^4\theta_{\mathrm{eq}}$, which has the same expression as K. This bending modulus, obtained from the minimization of total surface energies, has the same dependence on particle diameter, surface wettability, and interfacial tension as that adopted phenomenologically in other continuum models [7,24]. The length scale ℓ_e is equivalent to $(B/\Delta\rho g)^{1/4}$, the universal expression of wrinkle wavelength for a compressed thin elastic sheet on an elastic foundation [9,40].

With these scaling parameters, the nondimensional energy terms become

$$U_p^* = \mathcal{M}\int_0^{L^*} \eta^*\, ds^* + c_1, \tag{2a}$$

$$U_f^* = \frac{1}{2}\int_0^{L^*} \eta^{*2}\cos\alpha\, ds^*, \tag{2b}$$

$$U_i^* = \frac{1}{2}\int_0^{L^*} (\partial_{s^*}\alpha)^2\cos\alpha\, ds^* + c_2, \tag{2c}$$

where c_1, and c_2 are the constants that do not vary as the raft deforms, and $\mathcal{M}$ denotes the effective dimensionless weight of the particle layer [34]:

$$\mathcal{M} = \frac{\pi d^2\phi_s}{6\ell_e}\left[\frac{\rho_p - \rho_2}{\rho_1 - \rho_2} - \beta\right]. \tag{3}$$

Distinct from the existing continuum model [33], $\mathcal{M}$ in our model explicitly depends on the equilibrium position of particles at the fluid interface via β.

To find the equilibrium shape of the compressed particle array $\alpha(s)$, we minimize the total nondimensional energy $U^* = U_p^* + U_f^* + U_i^*$ under two constraints:

$$\Delta^* = \int_0^{L^*} \mathcal{P}(1-\cos\alpha)ds^*, \quad \partial_{s^*}y^* = \sin\alpha, \tag{4}$$

where $\Delta^* = \Delta/\ell_e$ is the imposed level of compression with an associated Lagrange multiplier $\mathcal{P}$, while the second constraint stems from the use of intrinsic coordinates. By following the energy minimization procedure described in Ref. [41], we obtain a single differential equation for the intrinsic angle $\alpha(s)$:

$$\partial_{s^*}^4\alpha + \partial_{s^*}^2\alpha\left[\tfrac{3}{2}\left(\partial_{s^*}^2\alpha\right)^2 - \tfrac{1}{2}\left[\partial_{s^*}^2\alpha(0)\right]^2 + \mathcal{P} - \mathcal{M}\eta^*\right] + \sin\alpha(1 - 2\mathcal{M}\partial_{s^*}\alpha) = 0. \tag{5}$$

For given Δ^* and $\mathcal{M}$, we numerically solve the system of equations using a continuation algorithm [7,41], subject to the free-floating boundary conditions [7]: $y^*(0) = y^*(L^*) = -\mathcal{M}$, $\alpha(0) = \alpha(L^*) = 0$.

Once the equilibrium shape of the raft is obtained, we plug it back into Eqs. (2a)–(2c) to calculate the total dimensionless energy U^* as a function of Δ^*. Note that we hereby drop the asterisk denoting the dimensionless variables for brevity. As shown in Fig. 3(c), the total raft energy U varies nonmonotonically with Δ for given $\mathcal{M}$, reaching a maximum before the localized fold in the particle array is close to self-contact. The nondimensional energy required to buckle a particle-laden interface is determined by the difference between the maximum U and $U(\Delta \approx 0)$, denoted as ΔU. As $\mathcal{M}$ denotes the dimensionless weight of the array, a lower degree of compression is required to localize the folds in the array with higher $\mathcal{M}$, resulting in lower ΔU.

Notably, we plot the results of our compression experiments described in Sec. II in terms of $\mathcal{M}$ to check if an all-encompassing nondimensional parameter can neatly organize the results from particle expulsion to buckling. We notice that an increasing $\mathcal{M}$ in Fig. 3(d) apparently indicates a transition from particle expulsion mode to interface buckling. However, it is not possible to identify a critical value of $\mathcal{M}$ that marks the transition from particle expulsion to buckling, as we observe both failure modes within the range $1.5 < \mathcal{M} < 2$, which correspond to the experiments with hexane-water and

hexane-brine. This again illustrates the limitation of a continuum approach alone to capture the raft's failure modes under compression.

B. Battle of two energies: A model of particle expulsion energy

In a jammed raft during compression, neighboring particles push on individual particles from all directions. The ability of a particle to stay attached to the interface depends on its initial stability and the motion of the three-phase contact line along its surface. To model the expulsion event in the simplest way possible, we neglect the effects of the neighboring particles and consider a spherical particle on a bare interface that is pushed quasistatically into the lower fluid [42] (Appendix C). The net downward force to detach the particle can be computed from the force balance, where the downward force F and the weight of the particle F_g must be balanced by the vertical component of the surface tension force F_γ acting at the three-phase contact line and the buoyancy force F_b [43]. For a spherical particle of diameter d, these forces are $F_g = -\pi d^3(\rho_p - \rho_2)g/6$, $F_\gamma = \pi d\gamma \sin\psi \sin\phi$, and $F_b = \pi d^3 \Delta\rho g(2h_\infty \sin^2\psi/d + 2/3 - \cos\psi + \cos^3\psi/3)/8$. We note that ψ and ϕ are the angular positions of the contact line relative to the center of the particle and the inclination of the interface with respect to the horizontal, respectively. We can use the geometrical relationship $\phi = \theta + \psi - \pi$ to replace ϕ with contact angle θ [43].

We nondimensionalize the lengths with the capillary length $\ell_c \equiv \sqrt{\gamma/\Delta\rho g}$ and the forces with $\Delta\rho g \ell_c^3$, so that the net downward force on the particle is given by

$$F^* = \frac{\pi d^{*3}}{8}\left(\frac{2h^*_\infty}{d^*}\sin^2\psi + \frac{2}{3} - \cos\psi + \frac{1}{3}\cos^3\psi\right) - \pi d^* \sin\psi \sin(\theta+\psi) - \frac{\pi}{6}Dd^{*3}, \quad (6)$$

where $D \equiv (\rho_p - \rho_2)/(\rho_1 - \rho_2)$. The net force, parametrized by the unknowns, θ, ψ, and h^*, can be derived by simultaneously solving for the shape of the fluid-fluid interface h^* via the Young-Laplace equation

$$h^*(r^*) = \frac{1}{r^*}\frac{\partial}{\partial r^*}\left(\frac{r^* h^*_{r^*}}{\sqrt{1+(h^*_{r^*})^2}}\right), \quad (7)$$

subject to the following boundary conditions:

$$h^*_{r^*}(r^* = d^* \sin\psi/2) = 0,\ h^*(r^* \to \infty) = 0. \quad (8)$$

Note that r^* is the radial distance from the center of the particle. The solution to Eq. (7) is obtained numerically by using a MATLAB routine "bvp4c" [44].

Once the force F^* and the instantaneous interfacial shape h^* are known as a function of the vertical position y^*, we estimate the work required for particle expulsion E^*_p by integrating F^* over the vertical distance. We separate the particle expulsion into two stages to account for the contact angle hysteresis: (i) the contact angle θ increases from the equilibrium contact angle θ_0 to the advancing contact angle θ_a, while the contact line remains fixed at $\psi = \psi_0$; (ii) once $\theta = \theta_a$, the contact line moves from ψ_0 until it detaches at the position ψ_d. Hence,

$$E^*_p = \int_{y^*_c(\theta_0)}^{y^*_c(\theta_a)} F^*\, dy^*\Big|_{\psi=\psi_0} + \int_{y^*_c(\psi_a)}^{y^*_c(\psi_d)} F^*\, dy^*\Big|_{\theta=\theta_a}, \quad (9)$$

where $y^*_c(\theta, \psi) = h^*_\infty(\theta, \psi) - d^* \cos\psi/2$ is the instantaneous position of the particle center; ψ_d is the contact line position upon detachment, which is set when F^* reaches a maximum value as a function of y^*_c. As before, we drop the asterisk denoting dimensionless variables for brevity.

Figure 4(a) is a representative plot at the hexane-water interface that shows how the particle expulsion energy E_p varies with particle diameter d rescaled by the hexane-water capillary length $\ell_c = 3.56$ mm. To calculate E_p from Eq. (9), the value of ψ_0 is obtained from the static equilibrium measurements, and θ_0 is found by solving the Young-Laplace equation with the initial static position of the particle at the interface (i.e., y_c, ψ_0) as the input. Due to the inherent variability in the particle

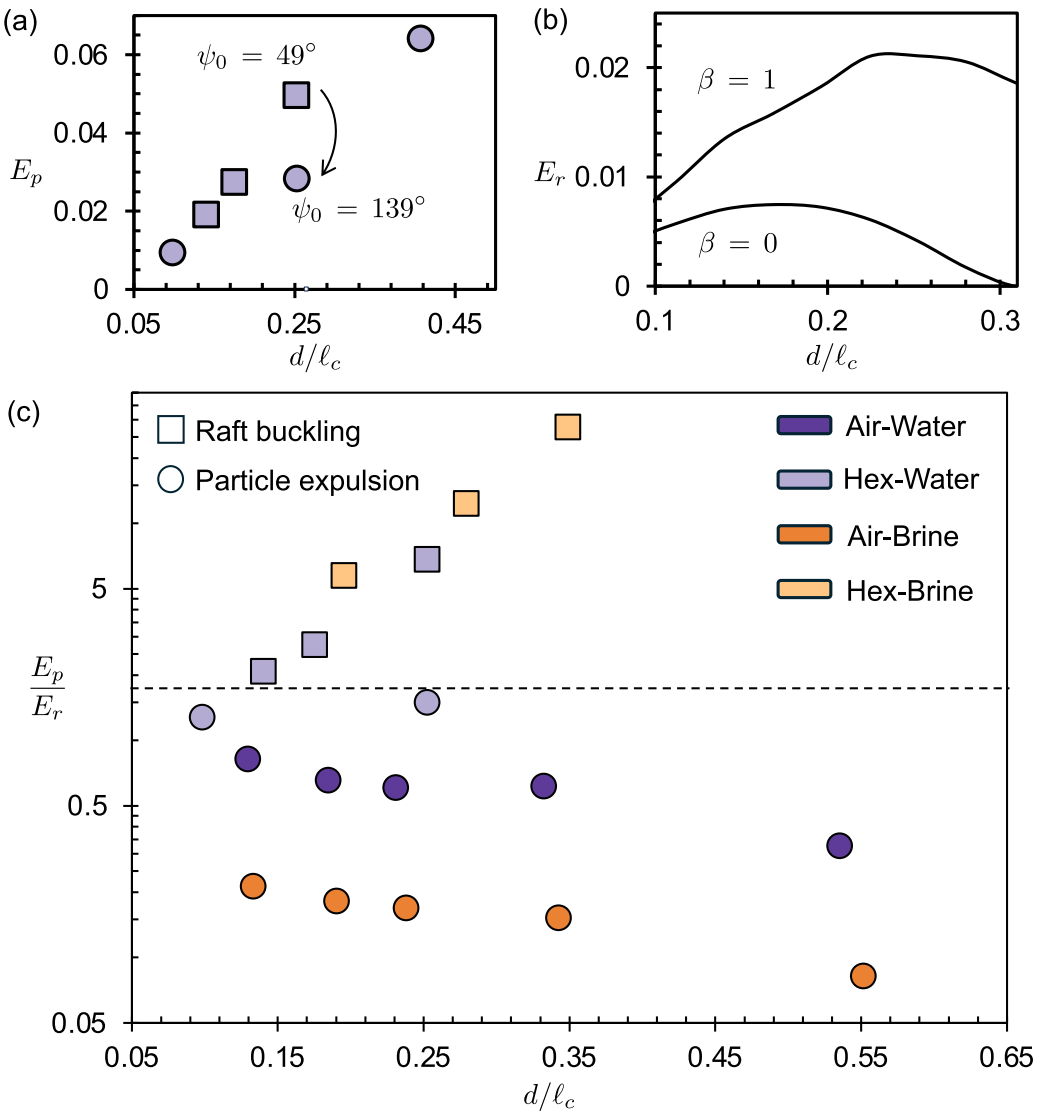

FIG. 4. Comparing the energies to fail a raft. (a) Nondimensional energy E_p to detach a particle from the hexane-water interface. E_p monotonically increases with nondimensional particle size d/ℓ_c. The change in equilibrium position for cleaned ($\psi_0 = 49°$) and unclean ($\psi_0 = 139°$) particles reflects in the decrease in E_p. Symbols for the energy values signify the corresponding raft failure mode. (b) Nondimensional energy to buckle a particle-laden hexane-water interface, E_r, changes nonmonotonically with particle size d/ℓ_c. For any particle position $0 < \beta < 1$, the energy to buckle a particle-laden hexane-water interface would fall between the two lines in the plot. (c) Phase map of different failure modes based on the energy ratio E_p/E_r and scaled particle size d/ℓ_c. For $E_p/E_r > 1$, the energy to expel a particle from the interface is more than the energy to buckle the interface. The experimental observations of buckling are all placed above the dashed horizontal line at $E_p/E_r = 1.8$.

surface, we acknowledge that θ_0 may differ from θ_{eq} that is measured in the wettability experiments with a glass slide (see Appendix B). In addition, as previously noted, the initial equilibrium position of the particle is sensitive to the particle release process itself, which can also contribute to the

deviation between θ_0 from θ_{eq}. In addition, we use θ_a from the dynamic particle removal experiments where we attach the particle at the end of a needle and quasistatically push it into the lower fluid (experimental details in Appendix C and Fig. 7). The results show that the particle expulsion energy increases monotonically with the particle size. At $d/\ell_c = 0.25$, making particle surface more hydrophilic lowers its equilibrium position ($\psi_0 = 49^\circ$ to 139°) and the energy required to remove the particle from the interface also decreases as expected.

C. The unified model to capture the dual nature of rafts

Finally, to compare the required buckling energy for the particle raft with the expelling energy for a single particle, we rescale ΔU from the continuum model to be consistent with the nondimensionalization of E_p in the particle model and label it as E_r. We again plot E_r as a function of d/ℓ_c for the representative case of a hexane-water interface in Fig. 4(b). We observe that the energy required to buckle an interface is higher when the particles are entirely submerged in hexane ($\beta = 0$) compared to when they are fully immersed in water ($\beta = 1$). At these extrema, the variation of E_r with particle size is nonmonotonic, i.e., it increases until a specific size but then drops to zero for particles more than a millimeter in diameter. As the particle positions will be in the range of $0 < \beta < 1$, the energy to buckle a particle-laden hexane-water interface would fall between the extrema.

We hypothesize that the raft dynamics are effectively determined by a competition between the energy terms E_p and E_r, and we compute their ratio E_p/E_r for all our experiments. Our experimental results for four different fluid-fluid interfaces, particle sizes, and surface wettabilities can then be compiled into a phase map of raft failure modes spanned by E_p/E_r and nondimensional particle size d/ℓ_c [Fig. 4(c)]. The dashed horizontal line at $E_p/E_r > 1$ demarcates the boundary between the particle expulsion and buckling failure as observed in the experiments. The transitional value of E_p/E_r corresponds to 1.8, which is $O(1)$ despite the simplicity of our composite model. This implies that the energetic cost of buckling must be comparable to that of single-particle expulsion, when the failure mode transitions from one mode to the other. The consistently low values of the energy ratio for both air-water and air-brine interfaces, irrespective of d, agree well with our experiments, where we have always seen single-particle expulsion at liquid-air interfaces. This is in contrast to a previous theoretical model [19], which predicted that increasing the particle size in a raft at the air-water interface would result in a transition from particle expulsion to buckling.

The map also incorporates the effect of particle surface wettability on raft dynamics. This essential factor is either ignored or rendered insignificant in existing continuum models of particle rafts [6,19,24]. Using a more wettable particle surface would result in a sharp drop in the value of the energy ratio, which explains the observation of single-particle expulsion at the hexane-water interface with $d \approx 900$ μm particles. Although not included in our phase map in Fig. 4(c), our model predicts that for mineral oil-water interfaces, the energy to buckle the interface is negligible, rendering a very high value for the energy ratio E_p/E_r. This is in perfect agreement with experiments, where, irrespective of particle size ($d \approx 90$ to 900 μm), buckling of the interface is the general mode of raft failure. For similar reasons, experimental results at the hexane-brine interface with $d \approx 900$ and 1450 μm are also excluded from the phase map, despite the model results aligning with the experimental observations. A reconstructed phase map with the energy ratio E_r/E_p (instead of E_p/E_r) and nondimensional particle size d/ℓ_c is included in Appendix D (Fig. 8), where we can locate the mineral oil-water and hexane-brine interface results at or near the zero-energy ratio in Fig. 8(b).

A few points warrant further discussion. First, our single-particle calculation provides a lower bound on E_p. Treating particle motion quasistatically, the model ignores the effect of viscous drag and the energy associated with the slipping of the contact line when the particle moves through the subphase fluid. These idealizations are justified in our study because, for the fluid interfaces used in the phase diagram of Fig. 4(c), the capillary number associated with the particle expulsion experiments is $\sim 10^{-5}$ signifying negligible viscous effects. Second, Fig. 2(f) shows that the energy barrier to buckling decreases with increasing $\mathcal{M}$ and eventually becomes zero. Physically, as $\mathcal{M}$

measures the effective weight of the particle raft relative to the effective restoring force (due to surface tension and buoyancy), the external energy required to buckle a raft would decrease with increased raft weight or decreased restoring force. Thus, our model predicts that the raft will collapse due to its weight beyond some critical $\mathcal{M}$, whose value could be better quantified via a complete three-dimensional raft model, outside the scope of this work. Finally, our model predicts nonzero energy input for expelling individual particles even when they float at the interface in a metastable state [44]. Future model modifications should also consider the effects of metastable floating conditions. Despite the approximations ignoring these subtle effects, our model accurately describes the macroscopic raft dynamics in experiments with a wide range of particle and fluid parameters, as evident from the phase map in Fig. 4(c) and Fig. 8 in Appendix D.

IV. ENGINEERING THE FAILURE MODE OF PARTICLE RAFTS

In addition to capturing the role of contact angle or static equilibrium position of particles, our model incorporates the effects of contact angle hysteresis. As per Eq. (9), the energy to quasistatically remove a particle from a fluid interface can be modified through the "stick-slip" motion of the contact line where the contact line initially remains stuck and suddenly depins to move between a series of pinning sites [45]. We hypothesize that if such a change is achieved without any appreciable change to the raft buckling energy E_r, the corresponding raft dynamics in compression will also change. Establishing this link between the three-phase contact line motion and the overall raft dynamics provides new insight, enabling us to modify the raft behavior through particle-scale manipulations.

As surface roughness can act as pinning sites [46–48], we roughen glass beads with $d \approx 900$ μm by rolling them between two pieces of sandpaper. Although the equilibrium position of an unaltered "smooth" glass bead is similar to that of a "roughened" glass bead at an air-water interface [Fig. 5(a)], the quasistatic particle expulsion experiments highlight their differences. Figure 5(b) compares the contact line motion on a smooth and a rough particle as it is expelled from an air-water interface (see Supplemental Material, movie S4). The images are created by superimposing four frames from respective particle expulsion experiments at specific intervals. For the smooth particle, the contact line moves along the particle surface, maintaining a constant contact angle. By contrast, contact line pinning is evident on the right side of the rough particle.

We quantitatively compare the contact line motion between the two particles by tracking the points L and R on the particle surface, shown by the green and black dots in the inset of Fig. 5(c). As evident from the superimposed contact line motion for the rough particle, tracking one point on either side of the particle ensures the spatial variability of the pinning locations is captured [42]. The position of the contact line is denoted by the angles ψ_L and ψ_R corresponding to points L and R, respectively. The result of tracking a smooth particle is plotted in Fig. 5(c). The green and black lines indicate the instantaneous position of the contact line over time. Their almost constant slope signifies an uninterrupted contact line motion as the particle pierces the air-water interface. Rafts made of these particles at the air-water interface always show single-particle expulsion, as depicted in the chronophotograph from the experiment in the inset of Fig. 5(c).

A stark difference is observed in the dynamic behavior of rough particles in Fig. 5(d). The variation of ψ_R signifies that the contact line remains stuck for an extended period and suddenly jumps to a higher advancing angle. The classic "stick-slip" motion on a roughened surface is evident in the variation of ψ_L. When these rough particles are used in a raft at an air-water interface, the raft fails via buckling instead of single-particle expulsion [Fig. 5(e)]. Thus, our experiments demonstrate how to engineer macroscopic raft behaviors by changing microscopic particle-scale features (Supplemental Material, movie S5).

To further explain our observation, we assume a model rough sphere where the local advancing contact angle is a sinusoidal function of the contact line position ψ given by $\theta = \theta_a + \theta_b \sin\{\pi[\psi - (\psi_p - 1)/2]\}[H(\psi_p - 1) - H(\psi_p + 1)]$, where the angle ψ_p points to the pinning location on the particle surface. Here, θ_b is the change of advancing contact angle due to a heterogeneous surface,

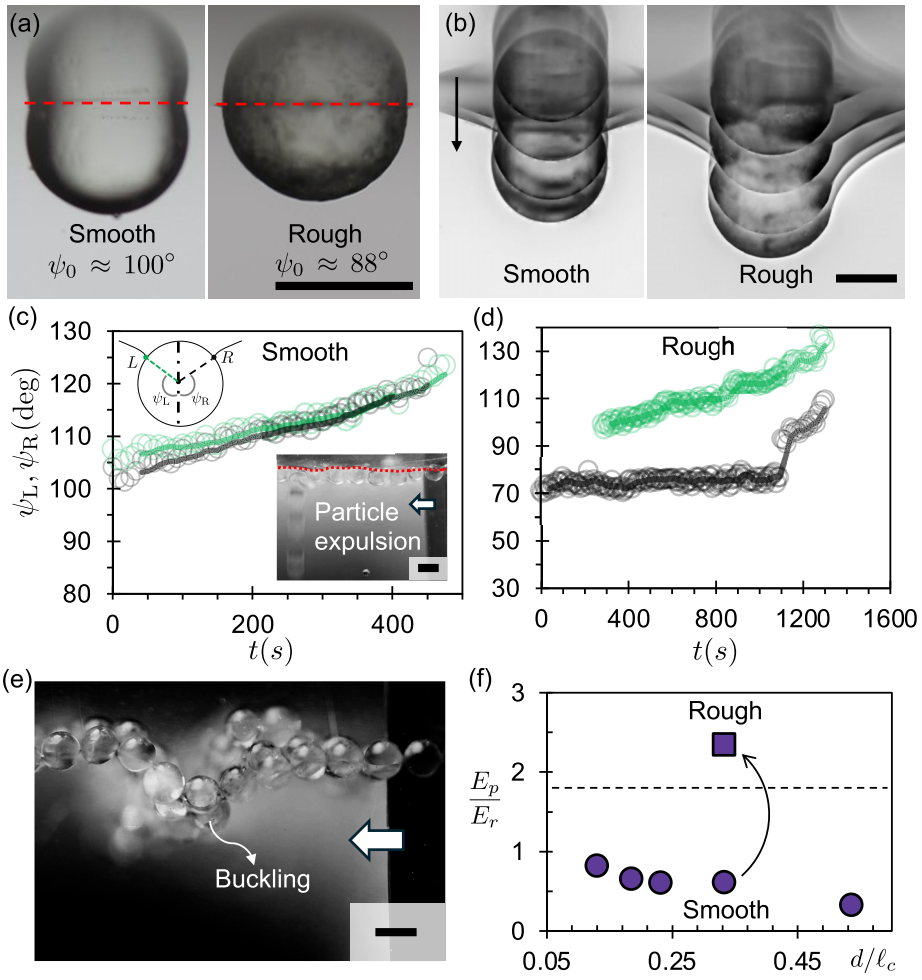

FIG. 5. Controlling raft dynamics. (a) Static equilibrium positions of a similarly sized smooth and rough glass bead at the air-water interface are comparable. (b) Superimposing four frames at a specific time interval from the dynamic particle expulsion experiments at the air-water interface shows the difference between a smooth and a rough glass bead. The contact line slides along the particle surface, maintaining a nearly constant contact angle as the smooth particle moves downward (indicated by the black arrow). In contrast, on the rough particle, the pinning of the contact line is evident from the significant deformation of the meniscus and the resulting change in the contact angle. (c) (Upper inset) The contact line is tracked with the right (R, black) or left (L, green) points on a particle as it pierces the interface. The location of the contact points is measured by the angle ψ on either side. The time-series plot of contact points on a smooth particle shows a continuous motion of the contact line. (Lower inset) A raft made of smooth particles fails via single-particle expulsion. The dotted red line shows the interface. (d) "Stick-slip" motion of the contact line is evident when a similar-sized rough particle is pushed through the air-water interface. (e) The raft made of rough particles fails via buckling at the air-water interface. (f) The model prediction shows that geometric heterogeneities on a particle surface increase the energy ratio E_p/E_r, confirming the experimental observation. All the scale bars are 1 mm.

and H is the Heaviside function, which ensures that the change of contact angle only occurs within $\pm 1^\circ$ of ψ_p. We set $\theta_b = 10^\circ$ and select five random ψ_p values as the pinning locations along the particle surface. The pinning and depinning of the contact line inevitably increases the particle expulsion energy E_p [Eq. ((9). As the interfacial properties (γ, $\Delta\rho$) along with the particle

equilibrium position (β) and diameter (d) remain unchanged, the raft buckling energy E_r for the smooth and rough particle is the same in our model. This pushes the energy ratio E_p/E_r for rough particles above the critical transition, indicated by the arrow in Fig. 5(f).

V. CONCLUSIONS

The crucial role of individual particles (e.g., their size, surface wettability, and contact angle hysteresis) in deciding the behavior of particle-laden fluid interfaces was known by the early 2000s [22]. Despite significant progress in understanding their characteristics and behavior since then [49], we still lack a first-principle analysis that connects the particle-scale behavior with the macroscopic raft dynamics. Our energy model, presented here, aims to fill this gap and predict the macroscopic raft dynamics in compression by analyzing the static equilibrium position and quasistatic motion of individual particles at the fluid interface. We have identified a criterion determining the raft failure mode during compression: if the energy required to detach a particle from the interface exceeds the energy to buckle a particle-laden interface, the raft would preferably fail by buckling. Informed by our model prediction, we show that the energies and, consequently, the failure mode of rafts can be controlled not only by particle size, surface wettability, or physicochemical modifications of the interface but also through their surface textures.

Although our study focuses only on rafts with larger particles, the theory presented here should generally apply to rafts of a wide range of particle sizes. The dynamics of colloidal particle-laden interfaces, both in the planar [50,51] and spherical [52,53] geometries, are often analyzed based on the area- or volume-dependent surface pressure variations, rather than the minimization of system energy. However, the surface pressure value is susceptible to the measurement methods [54], resulting in disparate conclusions about the general mechanism of colloidal raft destabilization [1,55]. Of course, as individual particle size reduces to colloidal or nanoparticle scale, the effect of line tension or thermal fluctuations in trapping the particles at the interface can be severe [56,57]. In addition, particle surface electrical charges or long-range capillary immersion forces will influence interface-mediated interactions between the particles and, consequently, the total free energy of the interface [58]. Allowing for these modifications in our analysis, our micro-to-macro energy model can predict the macroscopic behavior of generic particle-laden interfaces. From an engineering perspective, the phase map presented here provides a helpful framework for controlling the stability of particle-laden interfaces, which is relevant in applications requiring targeted fluid or particle delivery [21] and the arrest or triggering of ripening in foam and emulsion systems [59].

ACKNOWLEDGMENTS

This work was supported primarily by the National Science Foundation through the University of Minnesota MRSEC under Award No. DMR-2011401, and through Grants No. CBET-2032354 and No. CMMI-2042740. We are particularly grateful to E.-J. Puillet for providing insightful comments and generously sharing his methodologies and codes. R.M. also wants to thank Z. Kujala for suggestions, help in the experimental setup, and stimulating discussions.

X.C. and S.L. supervised the research. R.M., X.C., and S.L. designed the research. R.M. performed experiments and processed the data. R.M. and Z.-Y.C. analyzed the data. Z.-Y.C., X.C., and S.L. realized the theoretical model. All authors contributed to the manuscript writing.

There are no conflicts to declare.

APPENDIX A: PARTICLES AND FLUIDS

We have eight different mean particle diameters for particle rafts: $90 \pm 20\,\mu$m, $150 \pm 50\,\mu$m, $250 \pm 50\,\mu$m, $350 \pm 50\,\mu$m, $500 \pm 100\,\mu$m, $625 \pm 125\,\mu$m, and $900 \pm 100\,\mu$m, which we use in the plots in Figs. 2 and 4. Apart from these soda-lime glass beads, we have also used borosilicate glass beads (Mo-Sci Corp, $\rho_p \approx 2200\,\mathrm{kg/m^3}$, $d = 100 \pm 20\,\mu$m) for a few experiments.

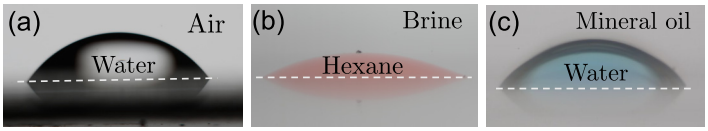

(d)

Upper fluid \ Lower fluid	Water	Brine
Air	55° ± 3°	74° ± 2°
Hexane	79° ± 9°	145° ± 11°
Mineral oil	47° ± 4°	-

FIG. 6. Wettability experiments. (a)–(c) The contact angle of different fluids on glass in varying fluid environments. The dashed white line denotes the position of the glass surface in all the images. (d) Table of contact angle values as measured from the experiments. The values are the average and standard deviation of three different measurements in each case.

Particles are prepared in three different ways to introduce the variability in the surface wettability of the particles: (1) using the particles as is, (2) rinsed, and (3) particles passed through a Piranha solution and sonicated for 10 min. The nonrinsed particles are usually very hydrophilic, as evident in their lower equilibrium position at an air-water interface. When these particles are first rinsed successively in a soap solution, regular tap water, and then distilled water, followed by drying in an oven for 4 h at 200 °C, their contact angle in water increases. The Piranha-treated particles are extremely hydrophilic as we could not form a raft with them.

Three different liquids are used as the heavier liquid phase in the experiments. These are distilled water ($\rho \approx 1000\,\mathrm{kg/m^3}$, $\gamma \approx 72\,\mathrm{mN/m}$), aqueous glycerol solution ($\rho \approx 1210\,\mathrm{kg/m^3}$, $\gamma \approx 58\,\mathrm{mN/m}$), and brine ($\rho \approx 1195\,\mathrm{kg/m^3}$, $\gamma \approx 81\,\mathrm{mN/m}$). The upper lighter fluids forming the fluid-fluid interface are air or hexane ($\rho \approx 655\,\mathrm{kg/m^3}$, $\gamma \approx 43\,\mathrm{mN/m}$). The values of density and surface tension in air for all these liquids are given within the parentheses. All the liquids except distilled water are from Sigma-Aldrich with 95%–99% purity. In the experiments where the surface tension of the water phase is lowered, we use 1.33-mM and 2.67-mM aqueous concentrations of sodium dodecyl sulfate (SDS, Sigma Aldrich).

APPENDIX B: WETTABILITY MEASUREMENTS

Due to the variability of our particle surfaces, we do not use a constant material contact angle value for defining particle equilibrium positions in our model. However, to calculate the interfacial energy contribution in the buckling energy analysis, a material contact angle value θ_{eq} is used for water on a glass surface in different fluids such as air, hexane, and mineral oil. For this, clean glass coverslips are selected because of their similar composition to our glass particles. Measuring the contact angle of water and brine on a glass slide in the air [Fig. 6(a)] or a mineral oil environment [Fig. 6(c)] is straightforward as water is the heavier fluid. The contact angle of wate and /brine on a glass surface in hexane is measured by placing upside-down glass slides wetted by hexane in a chamber filled with water and brine. When a glass slide wetted by hexane is placed in water, dewetting generates <2-μL droplets of hexane as shown in Fig. 6(b). We have tabulated the measurements in Fig. 6(d). All the angles are measured from the heavier fluid to the lighter fluid.

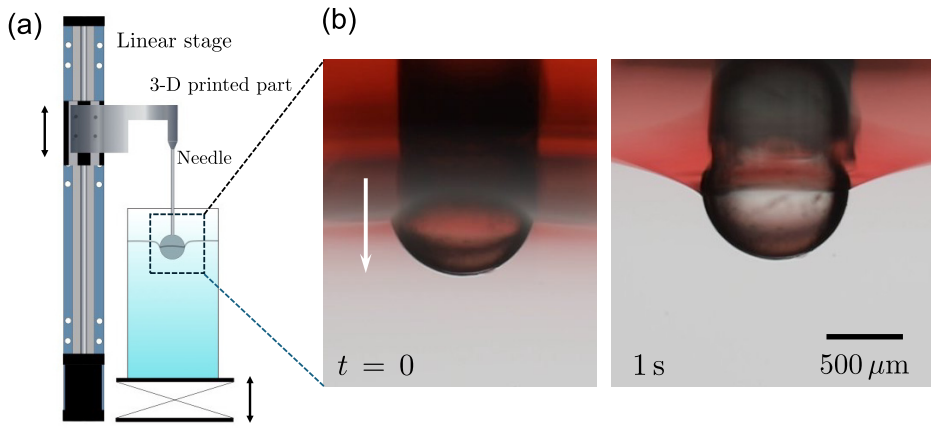

FIG. 7. Particle removal experiments. (a) A dynamic particle removal experiment was set up with a needle assembly attached to the sliding panel of a vertical linear stage. The particle is fixed to the end of the needle. (b) The equatorial plane of the particle is visible at the hexane-water interface in the $t = 0$ frame. The white arrow shows the direction of the needle-particle assembly movement. The contact line position and interface deformation are visible after 1 s.

APPENDIX C: DYNAMIC PARTICLE REMOVAL EXPERIMENT

We visualize the contact line dynamics over the particle surface as the particle leaves the interface, using the rectangular acrylic chamber (6.5 cm × 3 cm × 2.5 cm). We limit the experiments to particles with $d > 900$ μm for better visualization. As illustrated in the schematic in Fig. 7(a), one such particle is glued (glass glue or super glue, Loctite) to the end of a needle (22G or 21G dispensing needle, Dispense All), while the other end of the needle is locked in a custom 3D-printed fixture. This needle fixture is screwed to the sliding panel of a linear stage (FSL30, 100-mm stroke length, Fuyu). The linear stage speed and direction are adjusted with a digital stepper driver (DM320T, StepperOnline) and a stepper motor drive controller (15-160 VDC or 5-12 VDC, Sywan). The lowest speed setting is used for our experiments, roughly translating to a 750-μm/s linear speed of the needle assembly. Videos of particles piercing the interface are recorded at 120 fps with the help of a macro lens (Canon Mark IV fitted with a 65 mm 1–5× zoom). Time-stamped images from a representative experiment at a hexane-water interface with a ∼900-μm particle are shown in Figs. 7(b) and 7(c).

APPENDIX D: RECONSTRUCTED PHASE MAP

The phase map presented in Fig. 4(c) includes the results of particle raft behavior at four different fluid-fluid interfaces: air-water, hexane-water, air-brine, and hexane-brine. In addition, the particle surface wettability and size are also varied to capture the effects of a wide range of physicochemical parameters in dictating the macroscopic dynamics of a compressed raft. In our attempt to make the plot accessible, some experimental results could not be accommodated because the corresponding E_p/E_r ratio becomes too large or $E_p/E_r \to \infty$. In Fig. 8, we have reconstructed the phase map with E_r/E_p and d/ℓ_c. The data, expanded with experimental results at the mineral oil-water interface, show excellent agreement with our energy argument. Additionally, the buckling behavior of particle rafts at the hexane-brine interface with $d \approx 900$, 1450 μm is also visible below the critical energy ratio [see Fig. 8(b)].

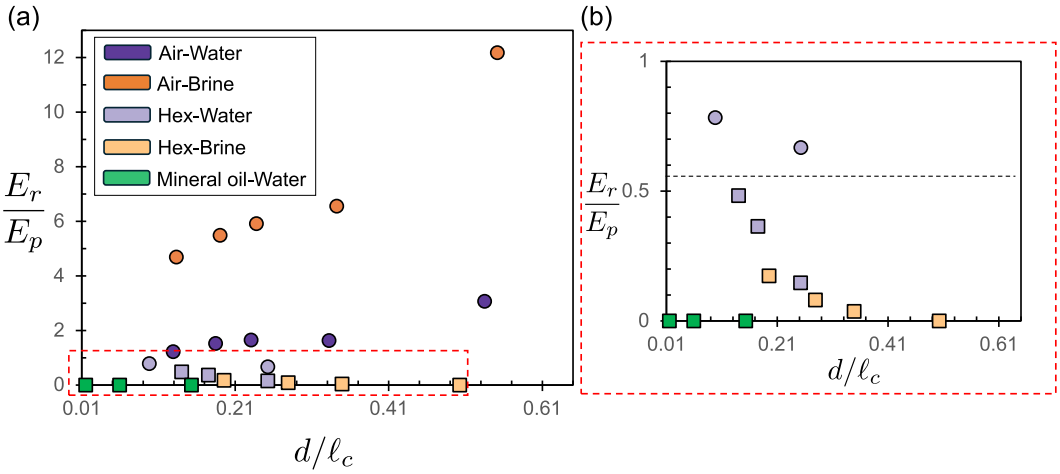

FIG. 8. Phase map of raft dynamics. (a) Reconstruction of the phase map in Fig. 3(c) with an inverse energy ratio E_r/E_p. Experimental observations for mineral oil-water (green) and larger particle data for the hexane-brine interface are shown here. (b) The dashed horizontal line shows the transition point between the two modes.

[1] R. Aveyard, J. H. Clint, D. Nees, and N. Quirke, Structure and collapse of particle monolayers under lateral pressure at the octane/aqueous surfactant solution interface, Langmuir **16**, 8820 (2000).

[2] D. Vella and L. Mahadevan, The "Cheerios effect", Am. J. Phys. **73**, 817 (2005).

[3] C. Monteux, J. Kirkwood, H. Xu, E. Jung, and G. G. Fuller, Determining the mechanical response of particle-laden fluid interfaces using surface pressure isotherms and bulk pressure measurements of droplets, Phys. Chem. Chem. Phys. **9**, 6344 (2007).

[4] B. D. Leahy, L. Pocivavsek, M. Meron, K. L. Lam, D. Salas, P. J. Viccaro, K. Y. C. Lee, and B. H. Lin, Geometric stability and elastic response of a supported nanoparticle film, Phys. Rev. Lett. **105**, 058301 (2010).

[5] S. S. Datta, H. C. Shum, and D. A. Weitz, Controlled buckling and crumpling of nanoparticle-coated droplets, Langmuir **26**, 18612 (2010).

[6] C. Planchette, E. Lorenceau, and A.-L. Biance, Surface wave on a particle raft, Soft Matter **8**, 2444 (2012).

[7] E. Jambon-Puillet, C. Josserand, and S. Protière, Wrinkles, folds, and plasticity in granular rafts, Phys. Rev. Mater. **1**, 042601(R) (2017).

[8] J. Huang, M. Juszkiewicz, W. H. de Jeu, E. Cerda, T. Emrick, and N. Menon, Capillary wrinkling of floating thin polymer films, Science **317**, 650 (2007).

[9] L. Pocivavsek, R. Dellsy, A. Kern, S. Johnson, B. Lin, K. Y. C. Lee, and E. Cerda, Stress and fold localization in thin elastic membranes, Science **320**, 912 (2008).

[10] See Supplemental Material at http://link.aps.org/supplemental/10.1103/ld9n-ctdh for the videos showing different raft dynamics under compression, varying fold positions during the raft's buckling failure, and the effects of particle roughness on the contact line dynamics and the raft failure mode under compression.

[11] B. P. Binks and T. S. Horozov, Aqueous foams stabilized solely by silica nanoparticles, Angew. Chem. Int. Ed. **44**, 3722 (2005).

[12] M. Abkarian, S. Protière, J. M. Aristoff, and H. A. Stone, Gravity-induced encapsulation of liquids by destabilization of granular rafts, Nat. Commun. **4**, 1895 (2013).

[13] S. U. Pickering, Emulsions, J. Chem. Soc. **91**, 2001 (1907).

[14] E. G. Schutt, D. H. Klein, R. M. Mattrey, and J. G. Riess, Injectable microbubbles as contrast agents for diagnostic ultrasound imaging: the key role of perfluorochemicals, Angew. Chem. Int. Ed. **42**, 3218 (2003).
[15] K. Stratford, R. Adhikari, I. Pagonabarraga, J.-C. Desplat, and M. E. Cates, Colloidal jamming at interfaces: a route to fluid-bicontinuous gels, Science **309**, 2198 (2005).
[16] M. E. Cates and P. S. Clegg, Bijels: a new class of soft materials, Soft Matter **4**, 2132 (2008).
[17] L. Bai, J. W. Fruehwirth, X. Cheng, and C. W. Macosko, Dynamics and rheology of nonpolar bijels, Soft Matter **11**, 5282 (2015).
[18] M. J. Razavi and X. Wang, Morphological patterns of a growing biological tube in a confined environment with contacting boundary, RSC Adv. **5**, 7440 (2015).
[19] B. C. Druecke, R. Mukherjee, X. Cheng, and S. Lee, Collapse of a granular raft: transition from single particle falling to collective creasing, Phys. Rev. Fluids **8**, 024003 (2023).
[20] S. Crossley, J. Faria, M. Shen, and D. E. Resasco, Solid nanoparticles that catalyze biofuel upgrade reactions at the water/oil interface, Science **327**, 68 (2010).
[21] V. Poulichet and V. Garbin, Ultrafast desorption of colloidal particles from fluid interfaces, Proc. Natl. Acad. Sci. USA **112**, 5932 (2015).
[22] Z. Hórvölgyi, M. Mate, A. Daniel, and J. Szalma, Wetting behaviour of silanized glass microspheres at water-air interfaces: a wilhelmy film balance study, Colloids Surf., A **156**, 501 (1999).
[23] V. Poulichet and V. Garbin, Cooling particle-coated bubbles: destabilization beyond dissolution arrest, Langmuir **31**, 12035 (2015).
[24] D. Vella, P. Aussillous, and L. Mahadevan, Elasticity of an interfacial particle raft, Europhys. Lett. **68**, 212 (2004).
[25] T. S. Horozov, B. P. Binks, R. Aveyard, and J. H. Clint, Effect of particle hydrophobicity on the formation and collapse of fumed silica particle monolayers at the oil-water interface, Colloids Surf., A **282-283**, 377 (2006).
[26] J. W. Tavacoli, G. Katgert, E. G. Kim, M. E. Cates, and P. S. Clegg, Size limit for particle-stabilized emulsion droplets under gravity, Phys. Rev. Lett. **108**, 268306 (2012).
[27] N. Taccoen, F. Lequeux, D. Z. Gunes, and C. N. Baroud, Probing the mechanical strength of an armored bubble and its implication to particle-stabilized foams, Phys. Rev. X **6**, 011010 (2016).
[28] C. Gu and L. Botto, Buckling vs. particle desorption in a particle-covered drop subject to compressive surface stresses: a simulation study, Soft Matter **14**, 711 (2018).
[29] P. A. Kralchevsky, I. B. Ivanov, P. Ananthapadmanabhan, and A. Lips, On the thermodynamics of particle-stabilized emulsions: Curvature effects and catastrophic phase inversion, Langmuir **21**, 50 (2005).
[30] Y. Nonomura and K. S., Surface activity of solid particles with extremely rough surfaces, J. Colloid Interface Sci. **317**, 501 (2008).
[31] P. Cicuta and D. Vella, Granular character of particle rafts, Phys. Rev. Lett. **102**, 138302 (2009).
[32] T. D. Kassuga and J. P. Rothstein, Buckling of particle-laden interfaces, J. Colloid Interface Sci. **448**, 287 (2015).
[33] S. Protière, C. Josserand, J. M. Aristoff, H. A. Stone, and M. Abkarian, Sinking a granular raft, Phys. Rev. Lett. **118**, 108001 (2017).
[34] E. Jambon-Puillet, Folds in floating membranes : from elastic sheets to granular rafts, Ph.D. thesis, Université Pierre et Marie Curie - Paris, 2016.
[35] O. Majérus, P. Lehuédé, I. Biron, F. Alloteau, S. Narayanasamy, and D. Caurant, Glass alteration in atmospheric conditions: crossing perspectives from cultural heritage, glass industry, and nuclear waste management, npj Mater. Degrad. **4**, 27 (2020).
[36] A. Varshney, A. Sane, S. Ghosh, and S. Bhattacharya, Amorphous to amorphous transition in particle rafts, Phys. Rev. E **86**, 031402 (2012).
[37] G. Lagubeau, A. Rescaglio, and F. Melo, Armoring a droplet: Soft jamming of a dense granular interface, Phys. Rev. E **90**, 030201(R) (2014).
[38] T. D. Gurkov and P. A. Kralchevsky, Surface tension and surface energy of curved interfaces and membranes, Colloids Surf. **47**, 45 (1990).

[39] P. A. Kralchevsky, J. C. Eriksson, and S. Ljunggren, Theory of curved interfaces and membranes: Mechanical and thermodynamical approaches, Adv. Colloid Interface Sci. **48**, 19 (1994).
[40] E. Cerda and L. Mahadevan, Geometry and physics of wrinkling, Phys. Rev. Lett. **90**, 074302 (2003).
[41] E. Jambon-Puillet, D. Vella, and S. Protière, The compression of a heavy floating elastic film, Soft Matter **12**, 9289 (2016).
[42] S. J. Kim, K. Fezzaa, J. An, T. Sun, and S. Jung, Capillary spreading of contact line over a sinking sphere, Appl. Phys. Lett. **111**, 134102 (2017).
[43] D. Vella, P. D. Metcalfe, and R. J. Whittaker, Equilibrium conditions for the floating of multiple interfacial objects, J. Fluid Mech. **549**, 215 (2006).
[44] D. Vella, D.-G. Lee, and H.-Y. Kim, The load supported by small floating objects, Langmuir **22**, 5979 (2006).
[45] D. Quéré, Wetting and roughness, Annu. Rev. Mater. Res. **38**, 71 (2008).
[46] J. H. Snoeijer and B. Andreotti, Moving contact lines: scales, regimes, and dynamical transitions, Annu. Rev. Fluid Mech. **45**, 269 (2013).
[47] J. F. Joanny and M. O. Robbins, Motion of a contact line on a heterogeneous surface, J. Chem. Phys. **92**, 3206 (1990).
[48] W. Ren and E. Weinan, Contact line dynamics on heterogeneous surfaces, Phys. Fluids **23**, 072103 (2011).
[49] S. Protière, Particle rafts and armored droplets, Annu. Rev. Fluid Mech. **55**, 459 (2023).
[50] S. Bordács, A. Agod, and Z. Hórvölgyi, Compression of langmuir films composed of fine particles: Collapse mechanism and wettability, Langmuir **22**, 6944 (2006).
[51] S. Razavi, K. D. Cao, B. Lin, K. Y. C. Lee, R. S. Tu, and I. Kretzschmar, Collapse of particle-laden interfaces under compression: buckling vs particle expulsion, Langmuir **31**, 7764 (2015).
[52] M. Abkarian, A. B. Subramaniam, S.-H. Kim, R. J. Larsen, S.-M. Yang, and H. A. Stone, Dissolution arrest and stability of particle-covered bubbles, Phys. Rev. Lett. **99**, 188301 (2007).
[53] O. Pitois, M. Buisson, and X. Chateau, On the collapse pressure of armored bubbles and drops, Eur. Phys. J. E **38**, 48 (2015).
[54] J. Kumaki, Monolayer of polystyrene monomolecular particles on a water surface studied by langmuir-type film balance and transmission electron microscopy, Macromolecules **21**, 749 (1988).
[55] G. Tolnai, F. Csempesz, M. Kabai-Faix, E. Kalman, Z. Keresztes, A. L. Kovacs, J. J. Ramsden, and Z. Hórvölgyi, Preparation and characterization of surface-modified silica-nanoparticles, Langmuir **17**, 2683 (2001).
[56] S. P. McBride and B. M. Law, Influence of line tension on spherical colloidal particles at liquid-vapor interfaces, Phys. Rev. Lett. **109**, 196101 (2012).
[57] E. Guzmán, F. Ortega, and R. G. Rubio, Forces controlling the assembly of particles at fluid interfaces, Langmuir **38**, 13313 (2022).
[58] O. S. Deshmukh, D. van den Ende, M. C. Stuart, F. Mugele, and M. H. G. Duits, Hard and soft colloids at fluid interfaces: Adsorption, interactions, assembly & rheology, Adv. Colloid Interface Sci. **222**, 215 (2015).
[59] P. J. Beltramo, M. Gupta, A. Alicke, I. L. D. Z. Gunes, C. N. Baroud, and J. Vermant, Arresting dissolution by interfacial rheology design, Proc. Natl. Acad. Sci. USA **114**, 10373 (2017).